The Astrophysical Journal, 894:20 (16pp), 2020 May 1 https://doi.org/10.3847/1538-4357/ab822c

A New Parameter of the Photospheric Magnetic Field to Distinguish Eruptive-flare Producing Solar Active Regions

Pei Hsuan Lin[1], Kanya Kusano[1], Daikou Shiota[2], Satoshi Inoue[1], K. D. Leka[1,3], and Yuta Mizuno[1]
[1] Nagoya University, Furocho, Chikusa-ku, Nagoya, Aichi, 464-8601, Japan; jnes40722@isee.nagoya-u.ac.jp
[2] National Institute of Information and Communications Technology (NICT), Nukui-Kitamachi 4-2-1, Koganei, Tokyo, 184-8795, Japan
[3] NorthWest Research Associates, Inc., Boulder, CO, USA
Received 2019 November 22; revised 2020 March 11; accepted 2020 March 19; published 2020 April 30

Abstract

Solar flares and coronal mass ejections (CMEs) are eruptive phenomena caused by coronal magnetic fields. In particular, large eruptive events originate in active regions (AR) with strong surface magnetic fields. However, it is still unclear what determines the capability of an AR to specifically produce eruptive flares and CMEs, and this hinders our knowledge of the initiation mechanism for the eruptive component of these phenomena. In this study, we propose a new parameter r_m to measure the possibility that a flare that occurs in an AR can be eruptive and produce a CME. The parameter r_m is defined by the ratio of the magnetic flux of twist higher than a threshold T_c to the surrounding—and specifically, the overlying—magnetic flux. The value of r_m for each AR can be estimated using nonlinear force-free field extrapolation models of the coronal magnetic field. Based on the data obtained by the Solar Dynamics Observatory/Helioseismic and Magnetic Imager, we calculated the values of r_m for 29 ARs at 51 times prior to flares larger than M5.0 class. We find that the footpoints of field lines with twist higher than 0.2 can represent the subsequent flare ribbons well, and field lines that overlie and "fence in" the highly twisted region will work to confine the eruption, generating confined flares. Discriminant function analysis is used to show that r_m is moderately well able to distinguish ARs that have the capability of producing eruptive flares.

Unified Astronomy Thesaurus concepts: Solar physics (1476); Solar magnetic fields (1503); Solar active regions (1974); Solar coronal mass ejections (310); Solar flares (1496)

1. Introduction

Coronal mass ejections (CMEs) and solar flares are abrupt releases of free energy that accumulated in the nonpotential fields through instabilities and magnetic reconnection. It is generally regarded that flares and CMEs are different manifestations of the same magnetic energy release process in the corona (e.g., Harrison 1995; Lin & Forbes 2000; Zhang et al. 2001; Priest & Forbes 2002; Harrison 2003; Zhang & Dere 2006; Maričić et al. 2007; Temmer et al. 2008; Cheng et al. 2010). Flares sometimes erupt with CMEs, but not all flares are accompanied by a CME. We refer to flares with CMEs as "eruptive flares" and to CME-less flares as "confined flares" in this study. The key property for determining whether a flare event will be eruptive or confined is not well understood. Previous studies showed that eruptive flares tend to have a higher peak flux in soft X-ray (SXR) observation (Cyr & Webb 1991; Harrison 1995; Wang 2002; Andrews 2003; Yashiro 2005). It has also been indicated that flares with longer duration have a higher probability of being eruptive events (Kahler et al. 1989; Kahler 1992; Harrison 1995; Cui et al. 2018). However, a number of exceptions indicates that flare properties measured from GOES observations are not the only factor that governs the eruptivity of a flare. For instance, Harra et al. (2016) found that among 42 analyzed X-class flares, there are not clear discriminators between the eruptive events and confined events when considering the event duration and GOES; Toriumi et al. (2017) statistically analyzed 51 $\geqslant$ M5-class flare events, finding that flare intensity and duration are not sufficient conditions to produce eruptive flares.

The surrounding magnetic field structure near the core region of solar eruptions is also suggested to play an important role in determining flare eruptivity. Torus instability (Kliem & Török 2006; Démoulin & Aulanier 2010) is one magnetohydrodynamic (MHD) instability that provides a possible scenario for CME-driving solar eruptions. It is suggested that if the core region is located where the magnetic field more quickly decays with height than a certain criterion, it is more possible to produce a CME (e.g., Fan & Gibson 2007; Liu 2008; Guo et al. 2010; Nindos et al. 2012; Jing et al. 2015; Wang et al. 2017; Baumgartner et al. 2018). Moreover, some studies indicate that strong magnetic fields lying above the flux rope will constrain its ascending motion and lead to confined flare events (e.g., Wang & Zhang 2007; Liu 2008; Cheng et al. 2011; Sun et al. 2015; Thalmann et al. 2015; Toriumi et al. 2017). In addition to the field strength, the topology of the surrounding field may also be associated with the eruptivity: DeRosa & Barnes (2018) found that intense eruptive flares ($\geqslant$X-class) tend to occur in regions near open magnetic field-line bundles. Many studies support the hypothesis that CME-poor events prefer to occur where background field lines are strong; however, the method by which to quantify how deeply the core structure is buried in the background field is still a topic of active research.

The formation mechanism of solar eruptions has long been an important topic in space science. Some properties of the coronal magnetic field in the pre-flare phase within the AR have been suggested to describe the condition required for forming eruptions. For instance, magnetic twist has been considered because it is related to the driving force of electric current-driven instabilities, such as the helical kink instability (Hood & Priest 1979; Einaudi & Hoven 1983). The kink instability occurs when the formed flux rope becomes unstable as the turn number of its helical field lines exceeds a certain threshold. On the other hand, Ishiguro & Kusano (2017) proposed the double-arc instability (DAI), specifying that double-arc shaped field lines that formed through tether-cutting reconnection (Moore et al. 2001) will become unstable when the value of the product of normalized reconnected flux and the twist

value in an AR, defined as κ, exceeds a certain threshold. Based on the DAI, Muhamad et al. (2018) used highly twisted field lines as a proxy of the reconnected field lines, finding that the DAI can be applied to observations in order to explain the onset of the solar eruptions. These approaches have shown that the magnetic field structure in the immediate vicinity of the highly twisted region is one important pre-eruptive signature. Although the accumulation of twist is a good indicator of solar eruption and flux rope formation, it is still challenging to directly relate the magnetic field twist to the generation of CMEs: Falconer et al. (2002) analyzed several global nonpotentiality measurements and their corresponding correlations to the CME productivities, finding that the higher global twist indicated higher CME productivity. However, Bobra & Ilonidis (2016) used the mean value of the force-free parameter as a proxy for the twist in their prediction method, but they found that it was not a sufficient condition for producing CMEs. Jing et al. (2018) analyzed the magnetic field structures in the pre-flare phase of 38 events, and find that the kink instability is not a necessary condition for eruptive flares. To sumarize, magnetic twist is a property associated with flare occurrences, but is not a sufficient condition for a CME. As a result, it is necessary to explore what additional conditions are needed to produce CME-accompanied flares.

It is widely regarded that the possibility of any given flare event to produce an eruption could be inferred by the equilibrium of the core regions and its surrounding magnetic field structure. The major objective of this study is to propose a new parameter that may be used to evaluate the capability of eruption by also considering the topological information of magnetic field structures, and the balance between the ascending force and the suppression force. In this paper, Section 2 presents the data and methods used in this research, and also the concept of the newly proposed parameter. Then, Section 3 introduces the parameter calculated from observations and a discussion of the results. Finally, Section 4 gives the summary and conclusions of this study.

2. Data and Methods

2.1. Event List and Methods

We use the events sampled by Toriumi et al. (2017); the data set was initiated by selecting the major flares that occurred in the period 2010 May–2016 April. These flares all have GOES SXR peak magnitudes in 1–8 Å bandpass $\geqslant 5 \times 10^{-5}$ W m^2 (M5.0). To reduce the effects from distortions due to projection effects, Toriumi et al. (2017) only included events located within 45° of disk center. Finally, 51 flare events from 29 active regions are arranged in Table 1. The CME association of each event is determined by reference to the CME catalog provided by the Solar and Heliospheric Observatory/Large Angle Spectroscopic Coronagraph.[4] The eruptive events are identified such that the CME onset time derived from the linear fitting to the height-time measurement according to the catalog agrees reasonably well with the flare onset time. Of these 51 flare events, 33 flares are eruptive and 18 events are confined. This eruptivity determination of each flare is also presented in Table 1.

In order to analyze the magnetic field structure of each flare event, we used Solar Dynamics Observatory (SDO)/Helioseismic and Magnetic Imager (HMI) observations of the vector magnetic field from the Spaceweather HMI Active Region Patch (SHARP; Bobra et al. 2014).[5] We used the `hmi.sharp_cea_720s` data, in which the vector magnetic field data has been remapped to a Lambert cylindrical equal-area (CEA) projection and decomposed into B_r, B_θ, and B_ϕ components and their associated uncertainty estimates. To examine the magnetic field structure at the pre-flare phase, the target for data analysis is approximately 1 hr prior to the start of each event.

In this study, nonlinear force-free field (NLFFF) extrapolations are implemented to reconstruct the coronal magnetic field structure. The MHD-relaxation method developed by Inoue et al. (2014) was extended to work in spherical coordinates as required for this study. We applied the INTERPOLATION function of IDL to reduce the resolution of the magnetogram to $0.^\circ14 \times 0.^\circ14$ in each pixel for the lower boundary of the NLFFF extrapolation. The potential field is required as the initial condition and boundary condition of the extrapolation, for which the potential field source-surface (PFSS) model (Altschuler & Newkirk 1969; Shiota et al. 2008) is initiated using the modified HMI synoptic chart of radial magnetic field (`hmi.Synoptic_Mr_720s`). As the synoptic charts are generated after every Carrington rotation (~27 days) is completed, we replace the target region with the SHARP data to ensure accuracy within the area under immediate consideration. The PFSS is calculated using a 1024-order spherical harmonic series expansion from the lower boundary (the modified synoptic chart) to the height of 2.5 solar radii. With this PFSS, we cropped out the wedge whose boundary was where the SHARP data were embedded into the synoptic chart. From this initial PFSS cube, the MHD-relaxation method gradually changes the horizontal component (B_θ and B_ϕ) at boundary through a set of MHD-like equations. We stop the iteration when the best-fit solution for all physical variables at the boundaries is achieved. The Lorentz force as well as the solenoidal condition within the numerical box is evaluated at the final step. Appendix A shows the consistency with a force-free field for for the computed models for each event. Finally, we numerically derive the three-dimensional coronal magnetic field. The numerical scheme we used in this study is the Runge-Kutta-Gill scheme with fourth-order accuracy for the temporal integrals and a central finite difference with second-order accuracy for the spatial derivatives. Figure 1 shows the reconstruction of the coronal field prior to the M6.6 flare event in AR 11158 on 2011 February 13 17:28 UT (event #1 from Table 1). Figure 1(a) shows the SDO/AIA 171 Å observation at the time roughly one hour prior to when the flare occurred on 2011 February 13 17:28 UT (event #1 listed in Table 1). Figure 1(b) shows the NLFFF calculation result for this event. The selected field lines plotted in this figure visually match the coronal loops in the AIA/171 Å image, and thus we propose that a model field captures the topological characteristics of this region's coronal magnetic field at this time.

2.2. Eruptivity and r_m

The balance between the outward force that drives the eruption and the inward force that restricts the eruption can be

[4] https://cdaw.gsfc.nasa.gov/CME_list/

[5] https://jsoc.stanford.edu/

Table 1
Event List for Analysis

Event#	GOES Start Time[a]	GOES Class[b]	Position[c]	NOAA#[d]	CME[e]
1	2011 Feb 13T17:28	M6.6	S20E05	11158	Y
2	2011 Feb 15T01:44	X2.2	S20W10	11158	Y
3	2011 Mar 9T23:13	X1.5	N08W11	11166	N
4	2011 Jul 30T02:04	M9.3	N14E35	11261	N
5	2011 Aug 3T13:17	M6.0	N16W30	11261	Y
6	2011 Aug 4T03:41	M9.3	N16W38	11261	Y
7	2011 Sep 6T01:35	M5.3	N13W07	11283	Y
8	2011 Sep 6T22:12	X2.1	N14W18	11283	Y
9	2011 Sep 7T22:32	X1.8	N14W31	11283	Y
10	2012 Jan 23T03:38	M8.7	N33W21	11402	Y
11	2012 Mar 7T00:02	X5.4	N18E31	11429	Y
12	2012 Mar 7T01:05	X1.3	N15E26	11429	Y
13	2012 Mar 9T03:22	M6.3	N15W03	11429	Y
14	2012 Mar 10T17:15	M8.4	N17W24	11429	Y
15	2012 May 10T04:11	M5.7	N12E22	11476	N
16	2012 Jul 2T10:43	M5.6	S17E06	11515	Y
17	2012 Jul 4T09:47	M5.3	S17W18	11515	N
18	2012 Jul 5T11:39	M6.1	S18W32	11515	N
19	2012 Jul 12T15:37	X1.4	S13W03	11520	Y
20	2013 Apr 11T06:55	M6.5	N07E13	11719	Y
21	2013 Oct 24T00:21	M9.3	S09E10	11877	Y
22	2013 Nov 1T19:46	M6.3	S12E01	11884	Y
23	2013 Nov 3T05:16	M5.0	S12W17	11884	N
24	2013 Nov 5T22:07	X3.3	S12E44	11890	Y
25	2013 Nov 8T04:20	X1.1	S13E13	11890	Y
26	2013 Nov 10T05:08	X1.1	S13W13	11890	Y
27	2013 Dec 31T21:45	M6.4	S15W36	11936	Y
28	2014 Jan 7T10:07	M7.2	S13E13	11944	N
29	2014 Jan 7T18:04	X1.2	S12W08	11944	Y
30	2014 Feb 4T03:57	M5.2	S14W07	11967	N
31	2014 Mar 29T17:35	X1.0	N10W32	12017	Y
32	2014 Apr 18T12:31	M7.3	S20W34	12036	Y
33	2014 Sep 10T17:21	X1.6	N11E05	12158	Y
34	2014 Sep 28T02:39	M5.1	S13W23	12173	Y
35	2014 Oct 22T01:16	M8.7	S13E21	12192	N
36	2014 Oct 22T14:02	X1.6	S14E13	12192	N
37	2014 Oct 24T21:07	X3.1	S22W21	12192	N
38	2014 Oct25T16:55	X1.0	S10W22	12192	N
39	2014 Oct 26T10:04	X2.0	S14W37	12192	N
40	2014 Oct 27T00:06	M7.1	S12W42	12192	N
41	2014 Nov 7T16:53	X1.6	N17E40	12205	Y
42	2014 Dec 4T18:05	M6.1	S20W31	12222	N
43	2014 Dec 17T04:25	M8.7	S18E08	12242	Y
44	2014 Dec 18T21:41	M6.9	S11E10	12241	N
45	2014 Dec 20T00:11	X1.8	S19W29	12242	Y
46	2015 Mar 10T03:19	M5.1	S15E39	12297	Y
47	2015 Mar 11T16:11	X2.1	S17E22	12297	Y
48	2015 Jun 22T17:39	M6.5	N13W06	12371	Y
49	2015 Jun 25T08:02	M7.9	N12W40	12371	Y
50	2015 Aug 24T07:26	M5.6	S14E00	12403	N
51	2015 Sep 28T14:53	M7.6	S20W28	12422	N

Notes.
[a] The start time of the flare according to the GOES catalog.
[b] Flare class from the GOES flare catalog.
[c] Flare location from the GOES flare catalog.
[d] Active region number assigned by NOAA.
[e] Y: eruptive event; N: confined event.

conceptually expressed as

$$r = \frac{F_{\rm driving}}{F_{\rm suppress}}, \quad (1)$$

where $F_{\rm driving}$ is the upward force acting on a flux rope formed by magnetic reconnection, and $F_{\rm suppress}$ is the downward-directed force that confines the eruption. Because it is challenging to estimate the amount of force directly from the

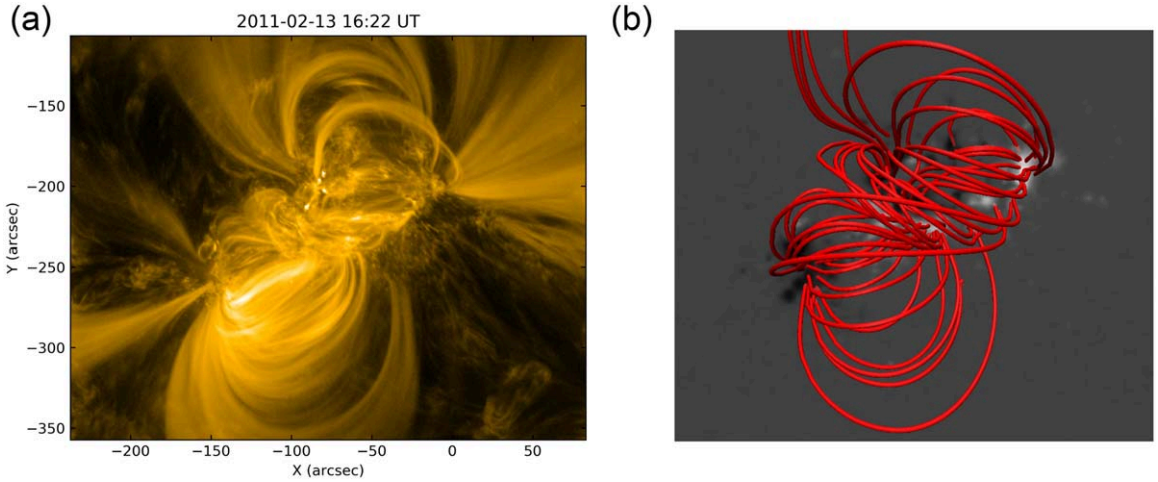

Figure 1. (a) SDO/AIA 171 Å observation of AR 11158 on 13 February 2011 16:22 UT. (b) NLFFF extrapolation result of AR11158. Red lines represent selected magnetic field lines from the NLFFF extrapolation.

observations, we propose that the force-balance parameter can be approximated by the ratio between the corresponding magnetic flux in the two systems:

$$r_m = \frac{\Phi_{\rm driving}}{\Phi_{\rm suppress}}, \tag{2}$$

such that a higher value of r_m indicates a higher possibility that an event will be eruptive. In this research we explore whether this parameter can help us infer whether an eruptive flare will be associated with the target reconnected flux rope.

The force that drives the eruption is regarded to be generated by the hoop-force on the reconnection-formed flux rope. This upward force will cause solar material to escape from the low solar atmosphere and thus lead to a CME. The source of this driving force most likely is the Lorentz force, which is generated by the electric current flowing along the magnetic flux rope after it is formed by magnetic reconnection. In this concept, $\Phi_{\rm driving}$ can be approximate by $\Phi_{\rm reconnect}$. To measure the reconnected flux from the observations, we must use another proxy to represent $\Phi_{\rm reconnect}$. Démoulin & Aulanier (2010) suggested that twisted field lines are more likely to cause internal magnetic reconnection and trigger the solar eruption. Furthermore, some studies have indicated that the flare ribbon patterns match the footpoints of the highly twisted field lines (Inoue et al. 2011, 2013, 2015). The statistical analysis implemented by Kazachenko et al. (2017) showed that the energy release of a flare, i.e., the reconnected energy, is strongly correlated with the magnetic flux that is cospatial with the flare ribbons, and the region swept by the flare ribbons has been shown to have a quantitative relationship with the magnetic reconnection process (Priest & Forbes 2002; Qiu 2009). The highly twisted field lines are therefore expected to be a good proxy of reconnected field lines. Muhamad et al. (2018) estimated the magnetic flux where the twist value was higher than a certain threshold (which modified κ as κ^*) to evaluate the stability for the DAI.

Regarding the denominator in Equation (2), we assume that the field lines that suppress the core region are mainly located nearby that region, and we refer to these field lines as "surrounding field lines." Moreover, highly twisted field lines themselves can also provide the suppressive force to confine the eruption. We hence modify (2) to

$$r_m = \frac{\Phi_{T_w \geqslant T_c}}{\Phi_{\rm surrounding} + \Phi_{T_w \geqslant T_c}}, \tag{3}$$

where $\Phi_{T_w \geqslant T_c}$ indicates the magnetic flux at the footpoints of the field lines that have a twist value (T_w) above a certain threshold (T_c), and $\Phi_{\rm surrounding}$ denotes the magnetic flux of the surrounding field lines. In our definition, $\Phi_{\rm surrounding} + \Phi_{T_w \geqslant T_c} = \Phi_{\rm suppress}$. To calculate the corresponding magnetic flux, we integrate the vertical magnetic field component over the area where the coronal footpoints are rooted in the photosphere.

The twist value of a field line is calculated from the following definition of magnetic twist (Berger & Prior 2006):

$$T_w = \frac{1}{4\pi} \int \alpha \, {\rm d}l. \tag{4}$$

Here, dl is a line element along a field line, and α is the associated force-free parameter, which is defined by

$$\alpha = \frac{\nabla \times \mathbf{B} \cdot \mathbf{B}}{|\mathbf{B}|^2}. \tag{5}$$

The twist value (T_w) is derived by integrating α over all of the voxels along each field line from one footpoint to the other. In a force-free construct, the α parameter is constant along each field line, and each footpoint can then be assigned a unique T_w. The twist value then describes the number of turns that the field line is wrapped around a central axis. In addition to the force-free construct, it is verified through a "blind test" that the twist value of an active region flux rope can be recovered from the magnetogram data based on evaluating the peak α corresponding to its axis (Leka et al. 2005). For each event, we calculate the T_w for every field line within the reconstructed box. In weak-field regions the large uncertainties for α makes the estimates of the twist values unreliable, hence we only consider the data where the radial component of the magnetic field strength exceeds 250 Gauss. The threshold of 250 Gauss is a somewhat conservative but otherwise arbitrary threshold above which the derived magnetic flux was not sensitive. Note that this threshold can also exclude data points with a weak horizontal field (<250 Gauss) at the same time.

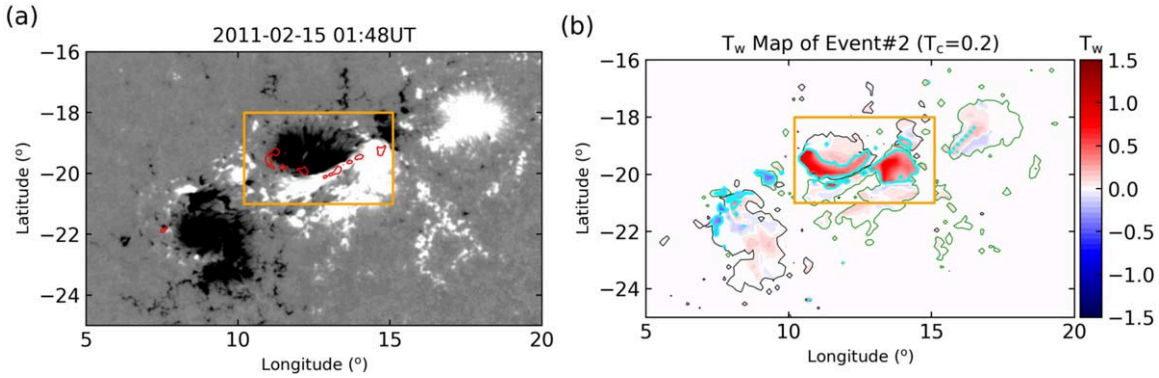

Figure 2. (a) AIA 1600 Å emission captured on 2011 February 15 01:48 UT, showing flare ribbon patterns (red contours), overlaid on a SHARP magnetogram at the same time (saturated at ±500 Gauss). The threshold used to highlight the emission patterns is the intensity that is equal to or higher than the mean value for 20σ (standard deviation) at a quiet-Sun time. (b) Twist map for AR 11158 calculated from an NLFFF extrapolation at a time corresponding to event #2 in Table 1. The cyan contours are the footprints of the field lines twist that exceed 0.2 turns ($|T_w| \geqslant 0.2$). the orange square in panels (a) and (b) highlights the region under consideration for r_m estimation.

2.3. Identification of Highly Twisted Field Lines

The estimation of r_m requires estimating both the flux of the highly twisted field lines ($\Phi_{T_w \geqslant T_c}$) and the flux of the field lines that surround them. As a result, this parameter strongly depends on the selection of the highly twisted field lines. Generally, flux tube models describe a group of coherent twisted structures that wind around a common axis, building a flux rope that is then related to an eruptive event. The region where this flux rope is rooted on the photosphere will form a pair of highly twisted regions conjugate along a magnetic polarity inversion line (PIL). However, in some active regions, multiple separated highly twisted regions may exist simultaneously and represent different flux ropes. Because in this situation the field lines wind around a different axis and would be responsible for different eruptions, we should not simply include all the regions with $T_w \geqslant T_c$ in case we incorrectly involve other regions that are unrelated to the targeted event. To correctly identify the targeted flux rope that should be used for the estimation of r_m for a particular event, we additionally take into account this flare's ribbons to find the appropriate footpoint region of the flux rope. Only field lines that have connectivity inside this region will be identified as the targeted flux rope for calculating r_m. We traced the field lines from multiple locations within each pixel on the lower boundary. In these extrapolated field lines a few field lines may obey the threshold, but connect away from the main body of the flux rope. We avoid including these field lines because they do not contribute to the main volume of the flux rope.

Figure 2 presents an example of the footpoint-area identification in the context of multiple possible twisted-region candidates. Figure 2(a) shows the initial brightening of flare ribbons inferred from SDO/AIA 1600 Å observations at 01:48UT. We highlight the region under consideration where ribbons appeared in the corresponding twist map at pre-flare time (Figure 2(b)). Because the twist value along a field line is uniquely assigned, the field lines across the PIL form a pair of conjugate patches in negative- and positive-polarity fields, which represent the footprints of the flux rope. In Figure 2(b), we find a pair of highly twisted patches with a similar shape to the flare ribbons. In Appendix B, we show all selected highly twisted regions (with $T_c = 0.2$) that are used to estimate the subsequent r_m parameter values. Throughout the study, we found that identifiable highly twisted patches inside an AR become recognizable only at $T_c \geqslant 0.2$. We therefore use $T_c = 0.2$ to choose the highly twisted regions of interest.

2.4. Discriminant Function Analysis

In this study, we aim to explore if two groups, eruptive flares and confined flares, are statistically different on the basis of r_m. Linear discriminant function analysis (DA; Leka & Barnes 2003) is a statistical method that can inform on the robustness of the hypothesis and quantify how exclusive these two groups are according to their measures of r_m.

The approach used by DA is to establish the function that best divides the parameter space given the known populations that are being sampled. In the case of the linear DA, the analyzed events are samples taken from two populations that are assumed to have normal distribution with the same covariances but different means. This technique estimates the probability function of the populations by fitting the samples with a parametric Gaussian distribution function. The discriminant boundary then locates where the two outcomes are predicated to occur at the same probability. In this this study, the samples are from two populations: one of eruptive events, and another of confined events. The discriminant boundary is located at the r_m value where the probability of an eruptive or confined event is equal. One may be concerned that Gaussian distributions may not represent the true population distributions. For example, magnetic flux is a purely positive quantity and hence is not well represented by a perfect Gaussian distribution. Nevertheless, Leka & Barnes (2007) have discussed how results may vary by relaxing the assumptions of linear DA, and argued that linear DA is appropriate for small sample sizes.

Because we have assumed the true population probability densities to be normal distributions with equal covariance matrices, we can therefore quantify the difference of the two fitted Gaussian distributions. To do this, we may use, for instance, the Mahalanobis distance, which is a normalized measure of the distance between the sample means. A significant Mahalanobis distance between the two samples indicates that they are likely drawn from different populations.

After establishing a discriminant function, we can present how well the function performs at classifying the two sets of samples by constructing a classification table, or a contingency table, that shows the correct and incorrect classifications. In

general, the threshold we use to construct the classification table is the value when two probability densities are equal, i.e., an identical possibility of observing eruptive and confined events. A variety of categorical statistics can be computed from the elements in the table, for instance, the true skill statistic (TSS or HKSS; Hanssen & Kuipers 1965), to describe the performance. With a single realization using all data points, each data point is used to classify itself, which will tend to underestimate the frequency of the incorrect predictions (Hills 1966). To remove this bias, we perform cross-validation: we remove one object from the samples and establish the discriminant boundary, then classify the excluded event. For a set with n samples, the procedure is repeated for $n - 1$ turns to finally provide an unbiased classification table. Considering the small sample sizes used in this study, we only present the results from using cross-validation.

3. Results and Discussion

3.1. Comparison of $\Phi_{T_w \geqslant T_c}$ and Φ_{Ribbon}

The magnetic field structure in the pre-flare phase has been reconstructed through NLFFF extrapolation for 51 analyzed flare events. Following the method described in Section 2.3, we derived the highly twisted magnetic flux based on different thresholds (T_c) in order to find the most appropriate threshold value that can best represent the reconnected magnetic flux. We compare the magnetic flux in the highly twisted area to the magnetic flux that is cospatial with the flare ribbons ($\Phi_{\rm Ribbon}$) provided by Toriumi et al. (2017). According to Toriumi et al. (2017), $\Phi_{\rm Ribbon}$ is the magnetic flux at the region swept by the ribbon observed in SDO/AIA 1600 Å. The pixels for inclusion are selected by the criteria of 40 standard deviation higher than the average 1600 Å intensity in the quiet-Sun area. $\Phi_{T_w \geqslant T_c}$ is the magnetic flux corresponding to the field lines with $T_w \geqslant T_c$ within the considered region. The calculated $\Phi_{T_w \geqslant T_c}$ with different T_c value are listed in Table 2. We also evaluated the expected sensitivity of $\Phi_{T_w \geqslant T_c}$ to the uncertainty in the magnetic boundary data through a Monte Carlo analysis. In this analysis, we repeated the same extrapolation on event #1 using 16 different sets of magnetic data in which we artificially add the error of observations at each pixel multiplied by a Gaussian-weighted random number with unity variance. The derived uncertainties of $\Phi_{T_w \geqslant 0.2}$, $\Phi_{T_w \geqslant 0.3}$, $\Phi_{T_w \geqslant 0.4}$, and $\Phi_{T_w \geqslant 0.5}$ are quoted in Table 2. Figure 3 shows the scatter plots of $\Phi_{T_w \geqslant T_c}$ and $\Phi_{\rm ribbon}$ with different T_c values. We used a linear correlation coefficient (CC) and the slope of the linear fit (r) to evaluate whether $\Phi_{T_w \geqslant T_c}$ represents the reconnected flux well. According to the results listed in Table 2 and shown in Figure 3, we find that both $\Phi_{T_w \geqslant 0.2}$ and $\Phi_{T_w \geqslant 0.3}$ are highly correlated with $\Phi_{\rm ribbon}$, but in the case of $\Phi_{T_w \geqslant 0.2}$, the value of r is much closer to 1. This suggests that the twisted flux represents the ribbon flux well when a threshold of 0.2 is used. Combining the results of CC and r, we conclude that $\Phi_{T_w \geqslant 0.2}$ is most representative for reconnected flux. With the criteria set at $T_c = 0.2$, we can identify highly twisted regions in the vicinity of the initial flare ribbons for all but one of the 51 events; the exception is studied in Section 3.4.

Following the same concept, Muhamad et al. (2018) used a much higher value of T_c to represent the reconnection flux.

Table 2
Highly Twisted Flux Based on Different T_c

Event#	$\Phi_{T_w \geqslant 0.2}$ $\pm 0.6\%$[a] (10^{20} Mx[a])	$\Phi_{T_w \geqslant 0.3}$ $\pm 0.9\%$ (10^{20} Mx)	$\Phi_{T_w \geqslant 0.4}$ $\pm 2.3\%$ (10^{20} Mx)	$\Phi_{T_w \geqslant 0.5}$ $\pm 2.5\%$ (10^{20} Mx)
1	29.52	24.81	18.82	8.65
2	36.54	29.68	21.8	14.21
3	17.93	10.38	4.96	1.07
4	7.27	3.24	2.75	1.51
5	18.77	11.83	7.7	3.84
6	25.9	17.17	10.44	1.39
7	13.8	7.88	4.9	1.22
8	15.53	11.41	8.41	5.91
9	12.48	10.41	7.7	5.84
10	2.91	1.95	0.54	0
11	136.77	92.38	56.39	22.38
12	124.61	88.86	50.53	21.87
13	122.62	76.97	32.72	11.13
14	37.66	24.03	12.67	1.79
15	6.31	5.77	4.91	3.56
16	4.8	1.85	0.17	0
17	4.61	3.34	1.4	0
18	4.24	4.08	1.54	0
19	67.46	43.77	30.53	7.71
20	5.51	1.02	0	0
21	6.42	6.42	5.52	2.71
22	10.24	7.62	6.24	3.13
23	5.67	4.49	2.21	0.97
24	10.74	7.36	4.92	3.9
25	8.05	4.72	0.39	0
26	9.88	8.62	8.35	6.84
27	20.83	10.49	2.95	0.71
28	10.87	8.01	6.24	4.83
29	0	0	0	0
30	33	22.16	15.15	12.05
31	11.57	7.69	4.62	1.9
32	5.33	1.01	0	0
33	48.11	16.95	5.2	0.24
34	35.88	18.57	0.29	0
35	121.1	76.24	30.99	10.72
36	158.06	87.6	33.71	8.19
37	111.71	47.51	8.43	0
38	40.56	24.44	10.87	0.84
39	32.33	26.17	16.41	3.11
40	43.25	29.09	15.25	3.06
41	42.54	27.09	14.72	7
42	5.55	0.85	0.26	0
43	67.96	34.68	8.69	1.17
44	47.47	33.28	15.3	7.33
45	66.9	36.92	18.13	2.65
46	5.16	3.48	1.39	0.82
47	9.66	6.89	5	3.58
48	71.05	50.94	39.19	30.91
49	48.04	28.77	8.21	0
50	0.75	0.75	0.75	0.3
51	5.66	4.18	2.31	1.03
CC[b]	0.782	0.748	0.664	0.39
r[c]	0.862	0.508	0.239	0.07

Notes.
[a] The uncertainties are presented assuming all magnetic fluxes estimated in event #1 are representative.
[b] Correlation coefficient between $\Phi_{T_w \geqslant T_c}$ and $\Phi_{\rm Ribbon}$.
[c] Slope of the linear regression line of $\Phi_{T_w \geqslant T_c}$ and $\Phi_{\rm Ribbon}$.

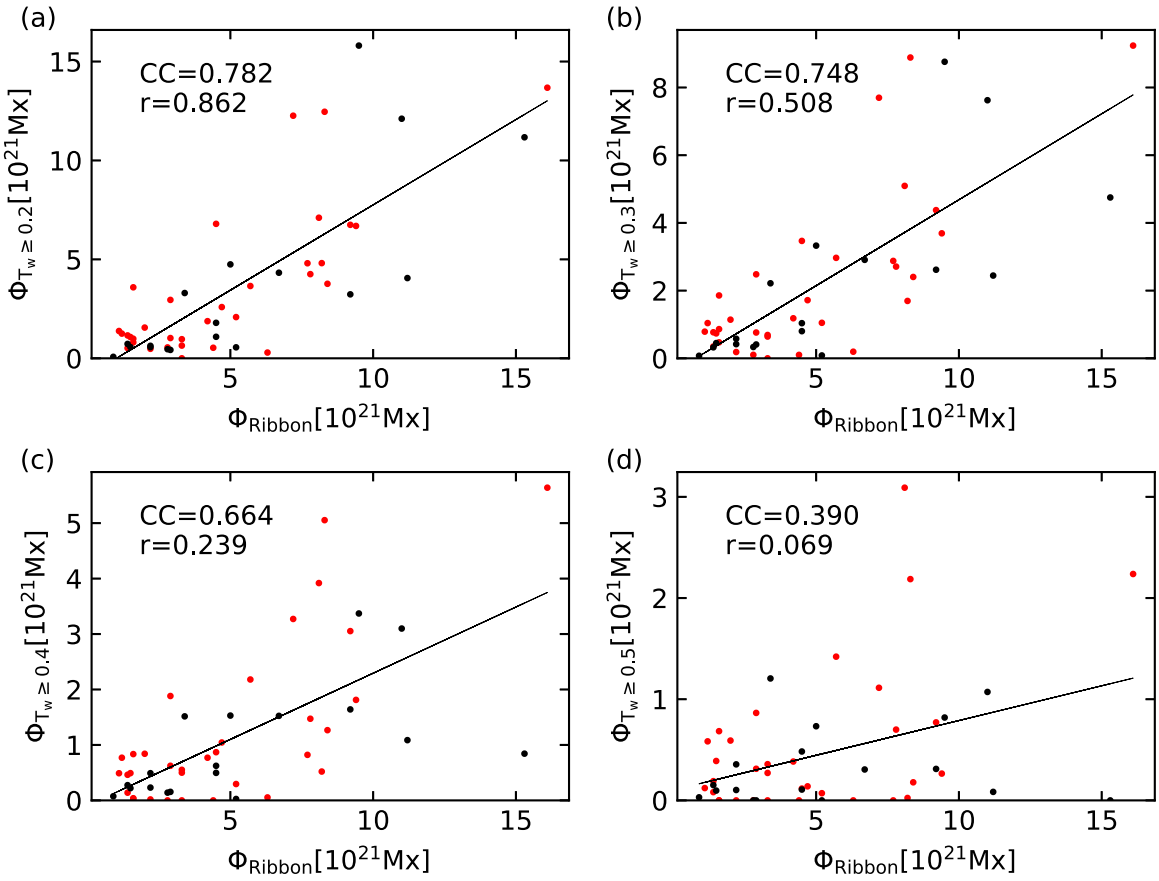

Figure 3. Scatter plots present the comparison of the magnetic flux within the twisted region $\Phi_{T_w \geqslant T_c}$) and the magnetic flux within the ribbon region ($\Phi_{\rm Ribbon}$) as calculated by Toriumi et al. (2017) for all 51 events. Red (black) dots represent eruptive (confined) events. The straight line shows the result of a linear fit, while the CC and the slope of regression line (r) are shown at the top left. Note the varying $y-$ scale.

According to Muhamad et al. (2018), different T_c values were tested and the most appropriate threshold was determined by examining the variation of κ^* with time during the flare eruption. The authors concluded that $T_c = 0.5$ was the most representative criterion for the reconnected field lines as κ^* drastically decreased after the flare occurs. However, in our study we find that $T_c = 0.5$ is not a suitable threshold under the assumption that $\Phi_{\rm reconnect} \simeq \Phi_{\rm Ribbon}$. We suggest that this discrepancy results from the different purposes of the two studies. We believe that the reconnected flux we estimate in this study focuses on all field lines that reconnected after the flare onset and contribute to the flux rope. Moreover, the flux estimated by Muhamad et al. (2018) corresponds to field lines that trigger the onset of the flare instead of all field lines provided by the magnetic field in the immediate vicinity. Figure 4 explains our theorem: the red field lines are those with a twist value over 0.5, and the yellow field lines are less strongly twisted. According to the tether-cutting model proposed by Moore et al. (2001), the core of the flux rope is formed by the inner reconnection of these strongly twisted field lines, which is illustrated in Figure 4(a). These red field lines are where the initial reconnection begins, after which the less strongly twisted field lines will also reconnect and become involved in the formation of the flux rope in the later phase (see Figure 4(b)). The double-arc instability focuses on the beginning phase of the flare (i.e., the triggering mechanism of the flare), therefore the twisted field lines at higher altitude (red field lines in Figure 4) are much more important. In this case, a higher threshold is required to select these field lines. However, the question we wish to solve here is whether the formed flux rope itself will be accelerated against the Sun. We therefore focus on the strength of this uplifting motion (estimated by $\Phi_{T_w \geqslant 0.2}$ in this study) and whether it can overtake the suppressive forces provided by the magnetic field in the immediate environs. We therefore use a lower value of T_c to include all the field lines in the immediate vicinity (both the yellow and red field lines shown in Figure 4).

3.2. Components of $\Phi_{\rm surrounding}$

The definition of $\Phi_{\rm surrounding}$ is still not well constrained because it has not been revealed yet what types of field lines will suppress the force of the eruption. In this study, we propose several possible hypotheses for its composition and use linear DA to test which is the most robust.

We defined surrounding field lines as those outside the core region that provide inward force to prevent the escape of the formed flux rope structure. The surrounding field lines may comprise a few components, as described by two hypotheses: first, there are numerous studies suggesting that overlying field can suppress the ascending eruption. We propose that $\Phi_{\rm surrounding}$ may be the flux corresponding to field lines that lie above the highly twisted region ($\Phi_{\rm surrounding} = \Phi_{\rm overlying}$). Our second hypothesis is based on the fact that the lifting of the core region will need to push out the lateral field to make a wide channel. We propose that the strength of the field lines

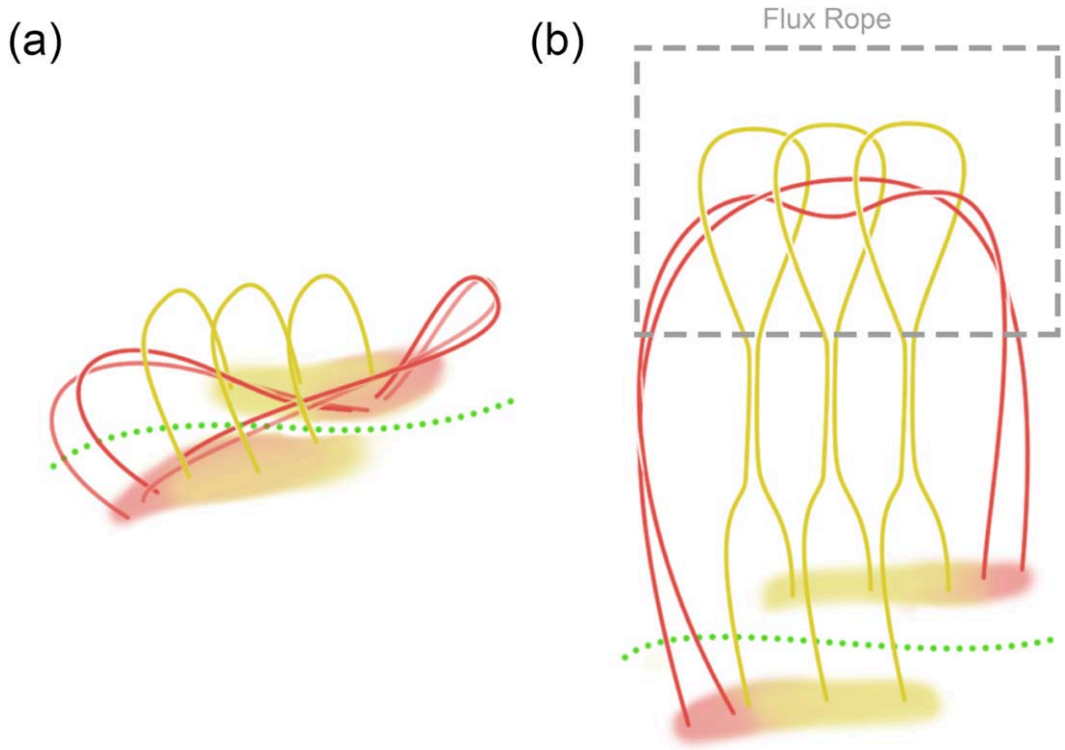

Figure 4. Schematic showing the topology of the field lines (a) before the onset of the eruption and (b) after the flare ribbons form. Red curves and red footpoints represent the highly twisted field lines that undergo tether-cutting reconnection and evolve into the magnetic flux rope. Yellow curves and their yellow footpoints are the slightly twisted field lines that strap the highly twisted field lines.

that form a fence around the core region will also relate to the eruptivity. We refer to these field lines as "wall" field lines, and the term $\Phi_{\rm surrounding}$ is composed of the overlying field *and* the wall field ($\Phi_{\rm surrounding} = \Phi_{\rm overlying} + \Phi_{\rm wall}$). The topologies of these field lines are explained in Figure 5, where wall field lines are those with one footpoint either beneath or near the growing core region of an eruption. After obtaining $\Phi_{T_w \geqslant T_c}$ and $\Phi_{\rm surrounding}$, r_m is calculated according to Equation (3). It is worth mentioning that some studies estimate similar quantities by calculating the transverse magnetic field across the PIL at higher altitude and the lower altitude, and estimate their ratio, which is similar to the concept of r_m (Wang & Zhang 2007; Liu 2008; Cheng et al. 2011; Sun et al. 2015; Thalmann et al. 2015). However, to precisely evaluate the balance and correctly define the morphology of the surrounding field, we attempt to select the field lines based on topological definition instead of only considering altitude. Regarding these two hypotheses, we use linear DA to test which is the most robust. This technique can provide some metrics to help us judge the performance of r_m in distinguishing eruptive events and confined events, and also help us check which hypothesis can separate two groups.

In our first hypothesis, the surrounding field lines are the overlying field lines. To select the overlying field lines, we project all field lines derived from NLFFF extrapolation onto the photosphere, choosing those that intersect the highly twisted field lines in the direction of gravity. We also remove those field lines that lie totally beneath the highly twisted field lines. The corresponding magnetic flux is then integrated over the relevant footpoints on the photosphere. Because the threshold 0.2 for the highly twisted region can well represent the reconnected flux, we determine the overlying field lines based on this threshold as well. The overlying field lines for event #1 are plotted as yellow curves in Figure 6. In the second hypothesis, the field lines near the core region are also included in $\Phi_{\rm surrounding}$. This type of field line will only have one footpoint near or possibly inserted beneath the highly twisted field lines, as shown in Figure 5. We thus define the wall field as those field lines in which only one footpoint is located near to the projection of the highly twisted field line, and the

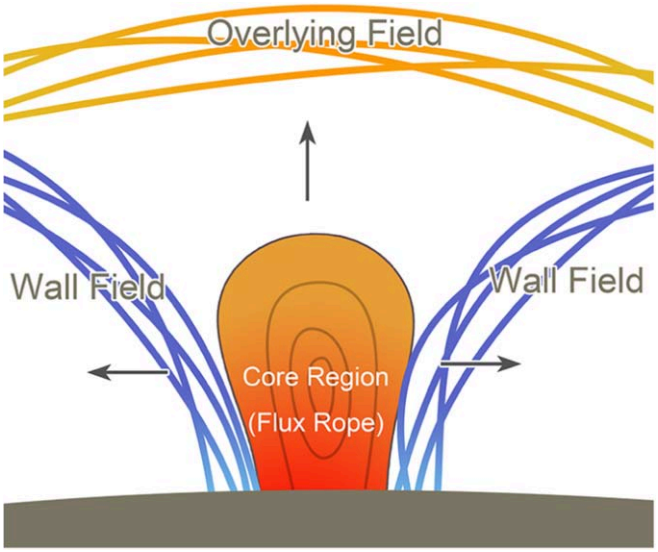

Figure 5. Schematic for overlying field lines and wall field lines. The red area located in the center represents the expanding core structure of the eruption. Black arrows indicate the expansion direction. Yellow and blue curves schematically show the relative location of the overlying field lines and wall field lines, respectively.

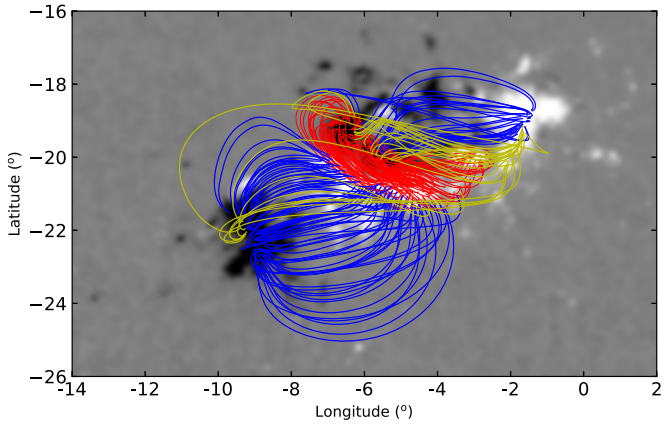

Figure 6. Curves illustrate the field lines selected according the thresholds described in Section 3.2. Following the color scheme in Figure 5, we show the overlying field lines (yellow), highly twisted field lines (red), and wall field lines (blue). The field lines are projected along the direction of gravity. The background is the interpolated photospheric magnetogram (saturated at ±500 Gauss) that served as the lower boundary condition of event #1.

threshold of the distance from the footpoint to the core region is 10 Mm. We establish this distance by maximizing essentially all metrics calculated from the linear DA when only that variable is varied. Figure 6 shows the topology of these projected wall field lines in event #1. After deriving $\Phi_{\rm surrounding}$, the r_m parameter is calculated separately based on the two hypotheses. We refer to the r_m value estimated according to hypothesis 1 as r_m^{h1} and to that estimated according to hypothesis 2 as r_m^{h2}. Table 3 lists all derived r_m^{h1} and r_m^{h2} in all analyzed events.

3.3. Performance of r_m and DA results

The DA results for r_m based on the two hypotheses are shown in Figure 7. The overlaid curves are the estimated probability density functions. The vertical blue line indicates the location where two probability densities are equal (which implies that the probability of eruptive flare is 50%) and it defines our discriminant boundary. Samples that lie to the right (left) of the boundary are assumed to be eruptive (confined) because the corresponding probability density function (PDF) lies above the confined (eruptive).

This shows that higher r_m is in fact related to a higher probability of producing an eruptive flare in both hypotheses. The metrics derived using DA are listed in Table 4. The higher value of the probability that two samples are from different populations for r_m^{h2} implies that using r_m^{h2} may better distinguish the two populations than r_m^{h1}. Despite the relatively high probabilities, however, the small sample sizes mean that the values are insufficient to definitively state that two distributions are from distinct populations. In parallel, the Mahalanobis distance for the sample PDFs is higher for r_m^{h2}, again implying that the underlying populations of r_m for confined events versus eruptive events becomes more exclusive when r_m^{h2} is used to discriminate the events. The classification tables constructed with n–1 cross-validation are presented in Tables 5 and 6. The correct rates and TSS statistics from the classification tables are summarized in Table 4. Both of these two metrics are higher when r_m^{h2} is used, indicating an improved classification ability when $\Phi_{\rm wall}$ is included in the calculation of r_m^{h1}.

Table 3
Estimates Related to r_m

Event#	$\Phi_{T_w\geqslant 0.2}$ ±0.6% (10^{20} Mx)	$\Phi_{\rm overlying}$ ±9.8% (10^{20} Mx)	$\Phi_{\rm wall}$ ±1.3% (10^{20} Mx)	r_m^{h1} [a] ±2%	r_m^{h2} [b] ±1%
1	29.52	6.45	51.29	0.82	0.34
2	36.54	8.21	93.55	0.82	0.26
3	17.93	40.15	25.65	0.31	0.21
4	7.27	9.31	11.23	0.44	0.26
5	18.77	16.16	24.53	0.54	0.32
6	25.90	12.52	32.70	0.67	0.36
7	13.80	5.61	16.74	0.71	0.38
8	15.53	6.57	16.19	0.70	0.41
9	12.48	13.48	17.50	0.48	0.29
10	2.91	17.32	3.78	0.14	0.12
11	136.77	144.36	17.88	0.49	0.46
12	124.61	144.58	24.63	0.46	0.42
13	122.62	107.94	12.76	0.53	0.50
14	37.66	52.18	27.03	0.42	0.32
15	6.31	18.58	36.44	0.25	0.10
16	4.80	6.91	15.36	0.41	0.18
17	4.61	21.47	65.38	0.18	0.05
18	4.24	24.13	68.58	0.15	0.04
19	67.46	75.98	77.16	0.47	0.31
20	5.51	5.22	13.45	0.51	0.23
21	6.42	7.16	14.06	0.47	0.23
22	7.45	12.13	22.97	0.38	0.18
23	5.67	14.17	9.54	0.29	0.19
24	10.74	28.55	59.92	0.27	0.11
25	12.31	68.21	12.64	0.15	0.13
26	9.88	25.97	25.87	0.28	0.16
27	20.83	15.55	43.14	0.57	0.26
28	10.87	62.11	48.35	0.15	0.09
29	0.00	0.00	0.00	0.00	0.00
30	33.00	31.23	61.51	0.51	0.26
31	11.57	4.49	3.17	0.72	0.60
32	5.33	15.32	13.09	0.26	0.16
33	48.11	67.60	15.24	0.42	0.37
34	35.88	35.54	61.11	0.50	0.27
35	121.10	137.76	185.04	0.47	0.27
36	158.06	132.80	202.44	0.54	0.32
37	111.71	98.00	187.26	0.53	0.28
38	40.56	89.32	186.15	0.31	0.13
39	35.74	44.45	197.15	0.45	0.13
40	43.25	52.51	239.52	0.45	0.13
41	42.54	38.69	29.68	0.52	0.38
42	5.55	29.71	21.26	0.16	0.10
43	67.96	21.99	52.87	0.76	0.48
44	47.47	33.83	19.79	0.58	0.47
45	66.90	81.90	45.94	0.45	0.34
46	5.16	0.56	11.31	0.90	0.30
47	9.66	14.35	63.24	0.40	0.11
48	71.05	65.79	20.47	0.52	0.45
49	48.55	73.60	31.12	0.40	0.32
50	0.75	12.59	11.73	0.06	0.03
51	5.66	22.75	46.91	0.20	0.08

Notes.
[a] r_m calculated based on hypothesis 1 ($\Phi_{\rm surrounding} = \Phi_{\rm overlying}$).
[b] r_m calculated based on hypothesis 2 ($\Phi_{\rm surrounding} = \Phi_{\rm overlying} + \Phi_{\rm wall}$).

To test the reliability of the resulting metrics from the DA, we estimate the corresponding uncertainties by performing Monte Carlo and bootstrap algorithms on our data set. First, for a Monte Carlo analysis, we perform the DA results on 10,000 sets of r_m^{h1} and r_m^{h2}. To generate these sets, we place an error that is arbitrarily drawn from the Gaussian-distributed random

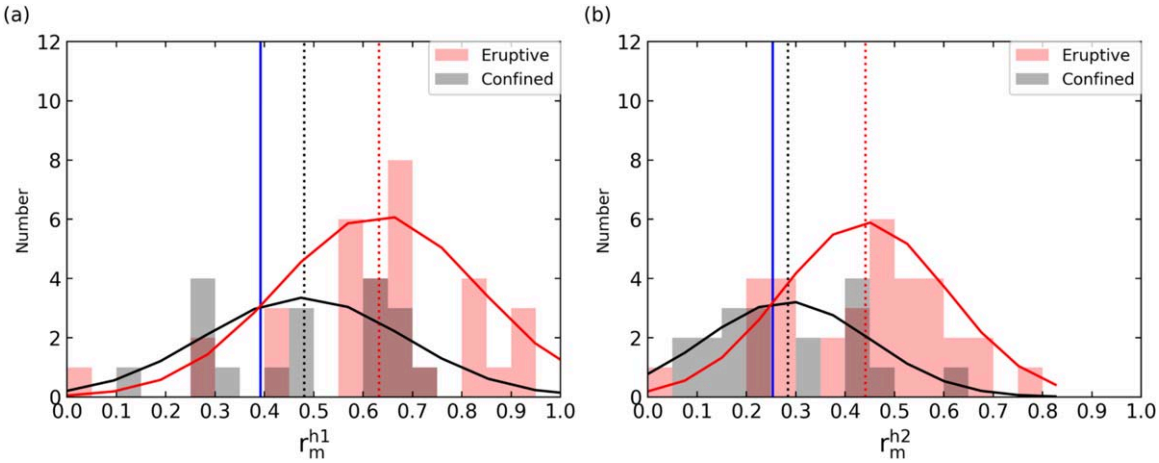

Figure 7. Linear DA results of r_m^{h1} and r_m^{h2}. The red (black) histogram represents the eruptive (confined) flares. Overlaid red (black) curves are the PDFs for eruptive (confined) flares. Red (black) vertical dash lines indicate the mean value of r_m for eruptive (confined) events. The point at which the two probability distribution functions are equal is denoted by the blue vertical line.

Table 4
DA Results (with n–1 Cross-validation)

Parameter	Mehod	Statistical Metrics			
		Probability (%)	MD[a]	CR[b]	TSS
r_m^{h1}	Original	94	0.63	0.65	0.15
	Monte Carlo	93.9 ± 0.4	0.63 ± 0.02	0.66 ± 0.01	0.17 ± 0.02
	Bootstrap	84.5 ± 17.4	0.59 ± 0.41	0.67 ± 0.07	0.14 ± 0.18
r_m^{h2}	Original	96.9	0.85	0.73	0.37
	Monte Carlo	96.9 ± 0.2	0.85 ± 0.02	0.73 ± 0.01	0.38 ± 0.02
	Bootstrap	89.8 ± 12.7	0.78 ± 0.57	0.69 ± 0.07	0.20 ± 0.19
$\lvert\Phi\rvert_{\rm Ribbon}/\lvert\Phi\rvert_{\rm AR}$	Original	97.2	0.88	0.67	0.07

Notes.
[a] Mahalanobis distance for the sample PDFs.
[b] Correct rate of the classification table.

Table 5
Classification Table (with n–1 Cross-validation) for r_m^{h1}

Observed	Predicted	
	Eruptive	Confined
Eruptive	27	6
Confined	12	6

Table 6
Classification Table (with n–1 Cross-validation) for r_m^{h2}

Observed	Predicted	
	Eruptive	Confined
Eruptive	27	6
Confined	8	10

numbers (with the standard deviation of the error values shown in Table 3) into the magnetic flux values and calculate the corresponding r_m^{h1} and r_m^{h2}. Second, using a bootstrap method, we reconstructed the samples by drawing with replacement 51 samples from the original data set to obtain a different resampled realization of samples. Each realization thus may include repeated samples, and present a different event rate. We repeat the resampling procedure 100 times, finally obtaining 100 sets of resulting DA metrics. The mean values and standard deviations provide the metrics and their uncertainties based on these two methods as summarized in Table 4. The expected small errors provided by the Monte Carlo method here arise because the uncertainties in the magnetic flux we derived in Section 3.1 are inherently small. The small uncertainties do not change the fitted PDFs or the discriminant function drastically, hence the DA results do not vary substantially. Compared to the Monte Carlo method, the bootstrap method measures the uncertainties from the sampling process, thus we can expect that it will provide a relatively large error due to the small sample size used in this study. We should consider the error provided by Monte Carlo methods as a lower bound and the error from the bootstrap method as an upper bound on the uncertainty estimates for the DA results.

We also carried out DA on the $\lvert\Phi\rvert_{\rm Ribbon}/\lvert\Phi\rvert_{\rm AR}$ provided by Toriumi et al. (2017). Due to the limited information available, we did not perform the error analysis on this parameter. The

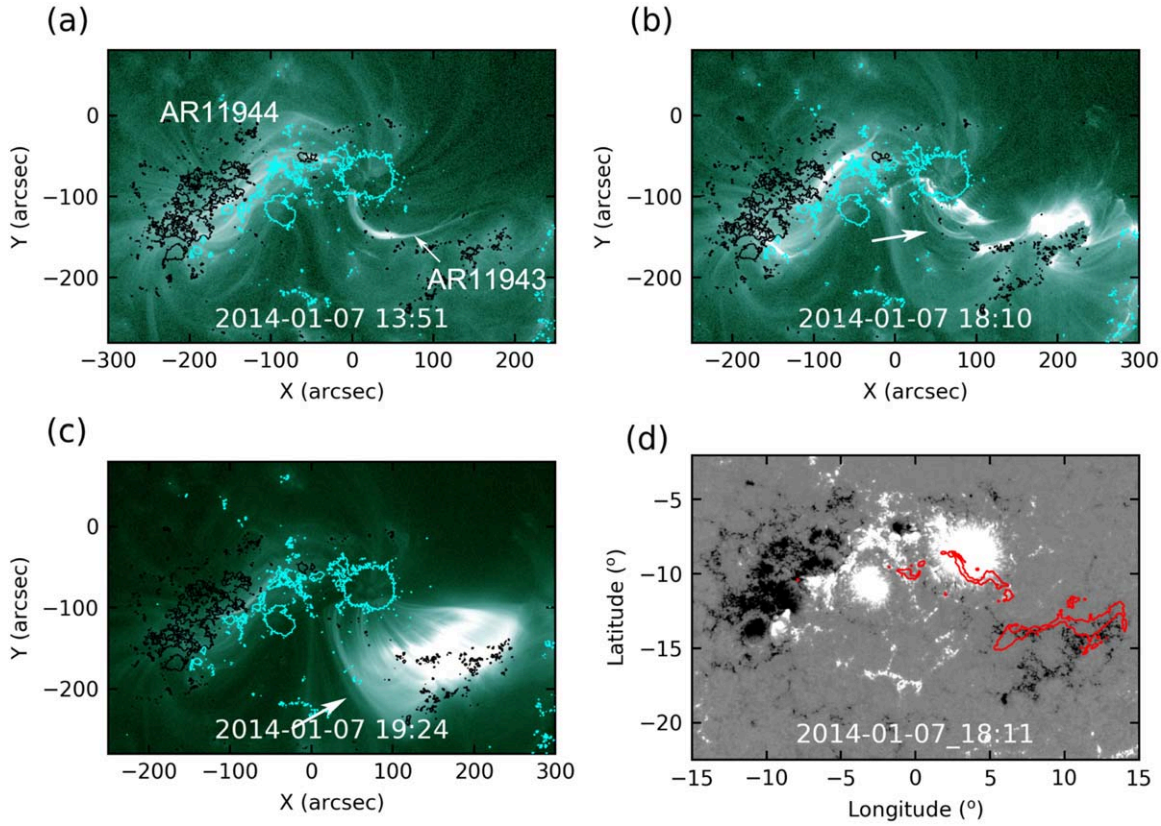

Figure 8. Panels (a)–(c) show the SDO/AIA 94 Å observations of AR11944 and AR11943 at three different times. The overlaid contours present the HMI magnetograms in the line-of-sight direction. The photospheric magnetic fields of −500 Gauss and 500 Gauss are marked by black and cyan contours, respectively. (a) The sigmoid that triggered the flare eruption captured one day before the eruption (January 6, 08:15UT). The white arrow indicates the position of the sigmoid. (b) The eruption of the sigmoid structure. The flaring location is indicated by the white arrow. (c) The post-flare arcade came up after the CME and flare erupted. (d) Ca II H line emission (highlighted by the same threshold mentioned in Figure 2) shown by the red contours overlaid on SHARP magnetogram data. The white and black shading corresponds to positive and negative polarities, respectively.

resulting metrics are shown in Table 4. The Mahalanobias distance and the probability derived based on $|\Phi|_{\rm Ribbon}/|\Phi|_{\rm AR}$ are comparable with the results of r_m^{h2}; however, the correct ratio and TSS derived based on $|\Phi|_{\rm Ribbon}/|\Phi|_{\rm AR}$ are significantly smaller than those derived based on r_m^{h1} and r_m^{h2}. This implies that the classification tables based on r_m^{h1} and r_m^{h2} can provide a better classifying ability than using $|\Phi|_{\rm Ribbon}/|\Phi|_{\rm AR}$. As a result, we can statistically conclude that using r_m^{h2} to classify the potential for eruptivity outperforms using $|\Phi|_{\rm Ribbon}/|\Phi|_{\rm AR}$.

Through the linear discriminant analysis, we find that neither r_m^{h1} nor r_m^{h2} are perfectly able to differentiate eruptive from noneruptive events, although r_m^{h2} may differentiate the events better. To examine one possibility of why this is the case, we next examine one of the incorrectly classified events in detail.

3.4. An Exceptional Event: X1.2 Flare on 2014 January 7

Although we can identify the highly twisted region in most of the events, for the X1.2 flare on January 7 (event #29 in our event list) that peaks at 18:32 UT, we failed to reconstruct any highly twisted region where flare ribbons appear, which contradicts our assumption that a highly twisted region will trigger the flare eruption. The flare occurred at S12W08 and was accompanied by a very fast CME: the projected speed reached $\cong$2400 km s^{-1} (Möstl et al. 2015). Figures 8(a)–(c) show the evolution of this event as seen in SDO/AIA 171 Å observations. The flaring position is roughly located between two ARs: AR11944 and AR11943. A coronal sigmoid links the two ARs and can be clearly seen on January 7 13:51UT (indicated by the arrow shown in Figure 8(a)), about one day before the flare onset. The sigmoid becomes faint just before the flare onset, thus we can hardly recognize the corresponding field line structures until the sudden brightening of the flare onset. Figure 8(b) shows the moment in which the sigmoid erupts (indicated by the white arrow). After the eruption, a post-flare arcade connecting the two ARs is formed (white arrow in Figure 8(c)) and the flare ribbons are observed afterward (red contours shown in Figure 8(d), from the AIA 1600 Å observation).

To further examine the magnetic structure of this event, we again compare the NLFFF results to the coronal structure as seen in AIA 171 Å observations. The selected extrapolated field lines plotted in Figure 9 present the magnetic field structure in the core region (red field lines) and the open field lines (white field lines). A bundle of open field lines is consistent with the structure captured in AIA 171 Å, but the red field lines are less strongly twisted than seen in Figure 8, implying that the extrapolation did not correctly reproduce the sigmoid that is expected to have initiated the eruption.

We speculate that the NLFFF extrapolation fails to capture the real coronal topology of this AR prior to this event. One possible reason is that the MHD relaxation finds the best-fit answer according to the observation at the photosphere, but in this case, the flare location is not near well-measured sunspots

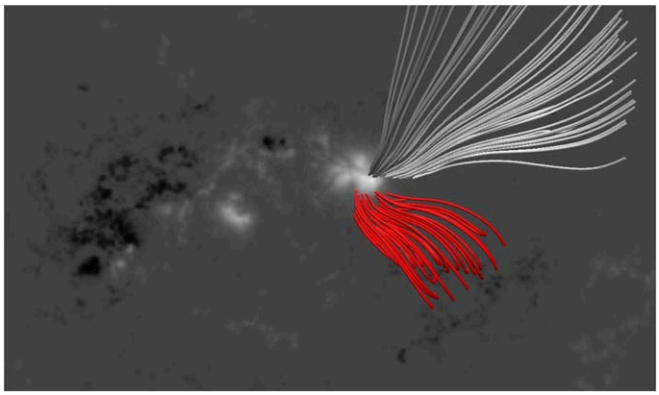

Figure 9. Selected NLFFF reconstruction of coronal field lines for event #19 at January 7 17:00 UT. The white field lines stand for the open field lines nearby the core region, while the red field lines are the reconstructed field lines where the initial flaring starts.

and the measurements may be poor. Second, the target flux rope has an extremely large spatial scale, which implies that it may also extend to very high altitude, beyond the normal bounds for the NLFFF extrapolation. Wang et al. (2015) also studied this AR and event, and tried to reconstruct the coronal field using a different NLFFF extrapolation method and boundary condition. The authors found that the flux rope, which was assumed to be ejected and become the CME, could not be reconstructed. They suggested that the flux rope was a very dynamic structure and that a model based on a static snapshot could not fully capture the real magnetic field structure.

4. Summary and Conclusion

We studied a parameter with the goal of helping to determine the potential for the eruptivity of a flare. In 51 analyzed flares with classification $\geqslant$M5.0, the coronal magnetic field structures are analyzed via NLFFF coronal magnetic field models prior to the event. We tested the hypothesis that eruptivity can be expressed as the equilibrium balance between the force that accelerates CME material and the downward force that confines any eruption. Using the parameter r_m to relate the balance of upward- and downward-directed forces, we tested the hypothesis that the force balance can be approximated by the ratio of the reconnected magnetic flux over the suppression flux. We conclude that r_m can provide a moderate ability for distinguishing the eruptive and confined events. We note that while we aimed to apply this parameter to CME forecasting, its predictive ability is restricted because it can only be determined when information of the flare ribbon location is provided (i.e., after the event has begun).

To estimate the reconnected flux before the eruption, we use the highly twisted flux as a proxy of the reconnected flux. Because Muhamad et al. (2018) indicated that this technique will be sensitive to the threshold (T_c) chosen to define the highly twisted flux, we compared how the highly twisted flux varies with different T_c to the ribbon flux in order to confirm the most appropriate T_c. We found that using a much lower threshold than expected ($T_c = 0.2$) may provide a proxy for the reconnection flux. This finding can be explained by the tether-cutting model proposed by Moore et al. (2001) because the model predicts that the less strongly twisted field lines will reconnect and build up the core region in the later phase of the eruption. Not only are the values of the highly twisted regions sufficiently representative of the ribbon flux, we also find that the footpoints of these field lines are spatially consistent with the ribbon pattern, which agrees with the results of a case study in Inoue et al. (2011).

In this study, we evaluate the ratio between repulsive force and the suppression force based on a morphological identification. According to the topological properties of field lines, two hypotheses are proposed and tested. By testing our hypotheses of the surrounding field lines, we found that not only the overlying field lines, but also the the wall field can confine the eruption process. Through a discriminant analysis (Figure 7), we demonstrate that by including the term $\Phi_{\rm wall}$, the eruptive events and confined events become more separated in the r_m parameter space. Furthermore, the classification performance (Tables 5 and 6) indicates that including the contribution of the wall field could improve the results.

However, there is a high degree of overlap between the two small sample sets. We suggest several factors that may reduce the difference between two groups: first, even as we have confirmed the structures computed by the NLFFF extrapolations by comparing the models to coronal observations, there might still be some invisible structures that are not yet captured by the NLFFF models because they do not follow the force-free assumptions (e.g., event #29 from Table 1). An inaccurate model will lead to an incorrect estimation of r_m. Second, as the selection of highly twisted region relies on manually identifying the target areas according to the flare ribbon locations, the overestimation or underestimation of $\Phi_{T_w \geqslant T_c}$ can cause an incorrect r_m. Finally, there may of course exist some other physical characteristics that have not yet been revealed. For example, magnetic structures in a far larger context around the eruption site may affect its eruptivity, as discussed in DeRosa & Barnes (2018).

We thank the SDO/HMI team for producing vector magnetic field data products. This work was supported by MEXT/JSPS KAKENHI grant No. JP15H05814. A part of this work was carried out using the computational resource of the Center for Integrated Data Science at the Institute for Space-Earth Environmental Research (ISEE), Nagoya University. Visualization of the NLFFF is produced by VAPOR (Clyne & Rast 2005; Clyne et al. 2007). The DA code is developed by Dr. Graham Barnes of NorthWest Research Associates (NWRA). K.D.L. acknowledges support by the US National Science Foundation under grant No. 1630454; any opinions, findings, and conclusions or recommendations expressed in this material are those of the authors and do not necessarily reflect the views of the National Science Foundation. P.L. acknowledges the Japan–Taiwan Exchange Association for supporting this study and stay in Nagoya University.

Appendix A
Force-freeness of the NLFFF Extrapolation

To confirm that NLFFF extrapolations are consistent with a force-free field, we evaluated the force-freeness and solenoidal condition of all extrapolated result through calculating $\langle {\rm CW}\sin\theta \rangle$ metrics and $\langle |f_i| \rangle$ metrics. These domain-averaged metrics have been used by DeRosa et al. (2009), and the values for all analyzed events are shown in Table A1. Because an ideal

force-free and divergence-free field requires $\langle \mathrm{CW}\sin\theta \rangle = 0$ and $\langle |f_i| \rangle = 0$, the small numbers of these two quantities shown in Table A1 suggest a consistency with the force-free and divergence-free condition in our extrapolation results.

Table A1
NLFFF Model Extrapolation Metrics

Event#	$\langle \mathrm{CW}\sin\theta \rangle$[a]	$\langle \lvert f_i \rvert \rangle$[b] ($10^{-6}$)
1	0.07	19.59
2	0.05	8.86
3	0.05	3.42
4	0.11	4.24
5	0.10	4.43
6	0.11	4.28
7	0.11	1.84
8	0.13	4.39
9	0.13	2.56
10	0.12	5.69
11	0.10	7.86
12	0.10	7.94
13	0.09	4.23
14	0.11	6.45
15	0.07	4.88
16	0.10	3.05
17	0.10	3.34
18	0.10	3.07
19	0.07	5.45
20	0.08	2.42
21	0.09	3.61
22	0.09	4.36
23	0.09	5.35
24	0.06	5.16
25	0.05	3.61
26	0.06	2.52
27	0.10	3.55
28	0.04	8.38
29	0.04	7.27
30	0.06	3.10
31	0.13	5.67
32	0.09	2.64
33	0.09	6.15
34	0.10	2.56
35	0.03	3.06
36	0.03	3.31
37	0.03	3.46
38	0.03	3.17
39	0.03	3.14
40	0.03	3.44
41	0.15	2.67
42	0.05	5.38
43	0.04	55.06
44	0.04	2.00
45	0.04	29.09
46	0.13	3.53
47	0.10	4.45
48	0.04	10.26
49	0.06	6.11
50	0.06	3.63
51	0.06	4.08

Notes.
[a] The $\langle \mathrm{CW}\sin\theta \rangle$ metric is the current-weighted average of $\sin\theta$, where θ is the angle between the magnetic and current vector. The data points with a signal-to-noise ratio ($|\boldsymbol{B}_i|/\sigma(\boldsymbol{B}_i)$) $\geqslant 3$ are denoted to be current-free when calculated.
[b] $|f_i| = |(\nabla \cdot \boldsymbol{B})_i|/(6|\boldsymbol{B}|_i/\Delta x)$ indicates the absolute fractional flux ratio at the pixel i, where Δx is the grid spacing.

Appendix B
Highly Twisted Regions for Estimating r_m

Figure B1 depicts all targeted highly twisted regions with $T_c = 0.2$ in the 51 analyzed events, identified following the steps described in Section 2.3. The selection of these regions is according to the ribbon pattern presented in Toriumi et al. (2017). Each subplot shows the SHARP B_r component (saturated at ± 500 Gauss). The overlaid (cyan) contours highlight the identified highly twisted region ($T_c = 0.2$) used in the estimation of r_m. Only in event #29 did we fail to identify any twisted field line with more than 0.2 turns.

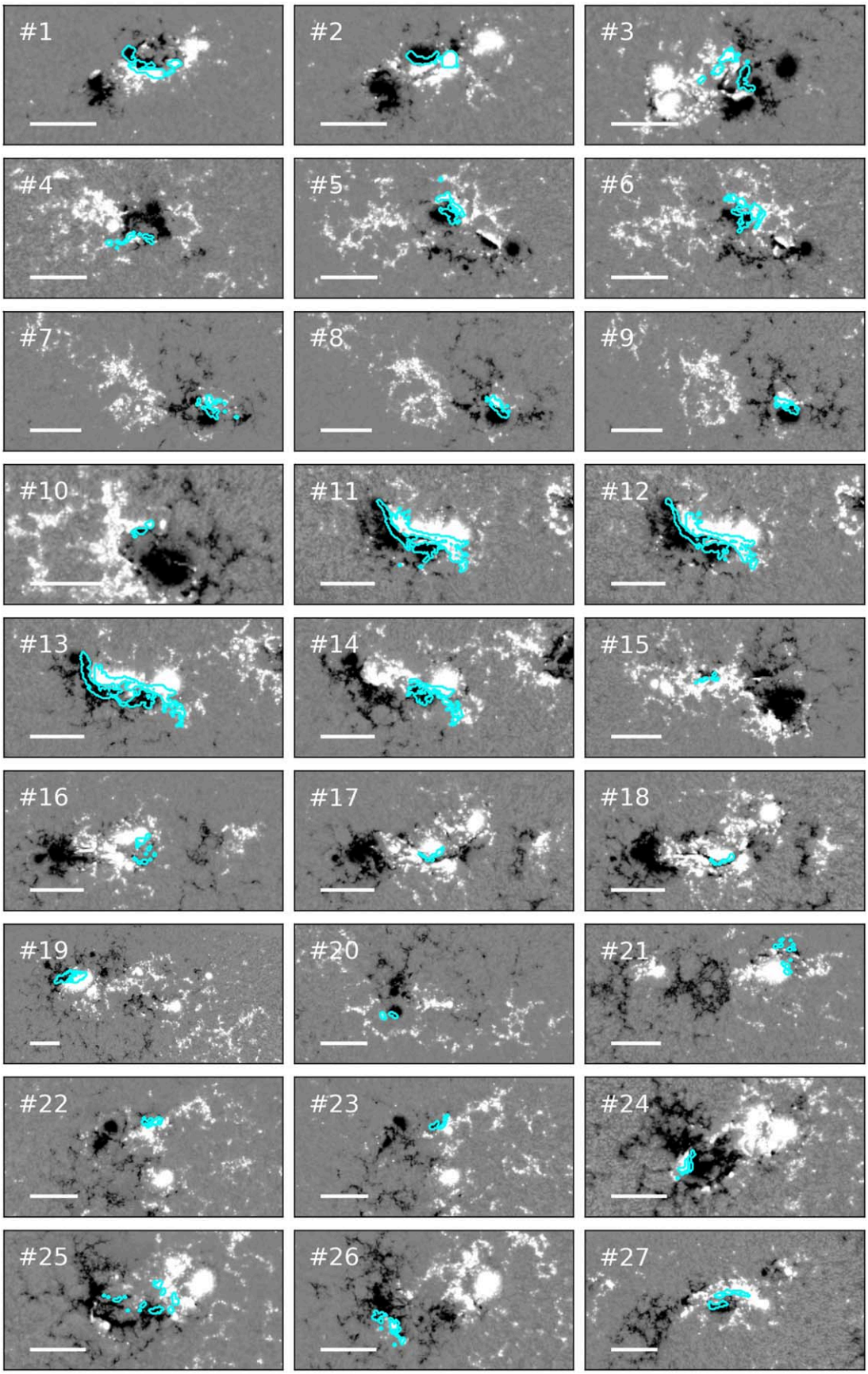

Figure B1. All events from Table 1 with the highly twisted regions used for analysis indicated. Background images are the B_r component that provides the boundary for the NLFFF extrapolation (saturated at $\pm$500 Gauss). The cyan contours indicate the regions selected to estimate the $\Phi_{T_w \geqslant T_c}$. The thick white line indicates the corresponding length of 5° in the CEA projection.

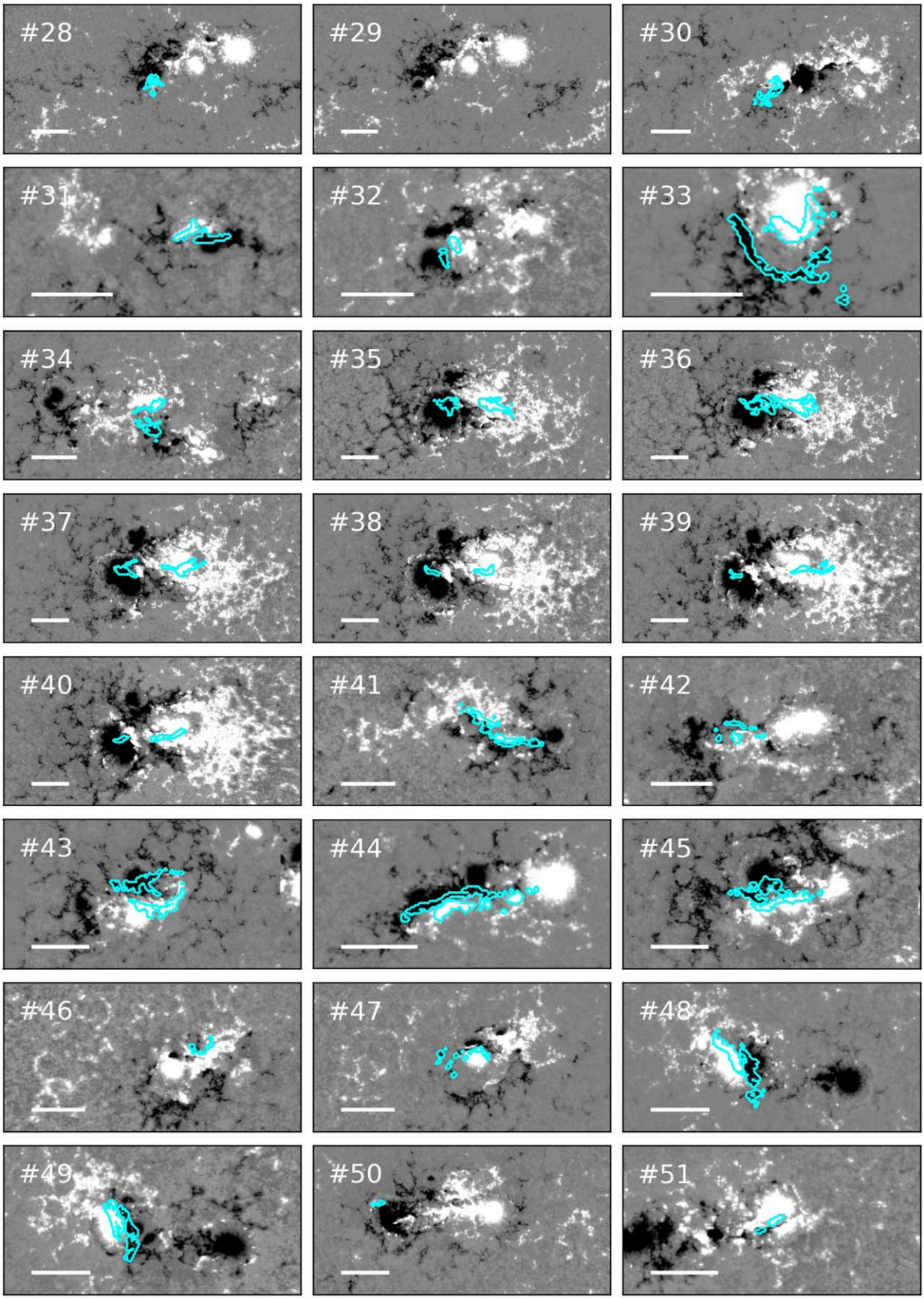

Figure B1. (Continued.)

ORCID iDs

Pei Hsuan Lin https://orcid.org/0000-0002-3873-7599
Kanya Kusano https://orcid.org/0000-0002-6814-6810
Daikou Shiota https://orcid.org/0000-0002-9032-8792
K. D. Leka https://orcid.org/0000-0003-0026-931X

References

Altschuler, M. D., & Newkirk, G. 1969, SoPh, 9, 131
Andrews, M. 2003, SoPh, 218, 261
Baumgartner, C., Thalmann, J. K., & Veronig, A. M. 2018, ApJ, 853, 105
Berger, M. A., & Prior, C. 2006, JPhA, 39, 8321
Bobra, M. G., & Ilonidis, S. 2016, ApJ, 821, 127
Bobra, M. G., Sun, X., Hoeksema, J. T., et al. 2014, SoPh, 289, 3549
Cheng, X., Zhang, J., Ding, M. D., Guo, Y., & Su, J. T. 2011, ApJ, 732, 87
Cheng, X., Zhang, J., Ding, M. D., & Poomvises, W. 2010, ApJ, 712, 752
Clyne, J., Mininni, P., Norton, A., & Rast, M. 2007, NJPh, 9, 301
Clyne, J., & Rast, M. 2005, Proc. SPIE, 5669, 284
Cui, Y., Wang, H., Xu, Y., & Liu, S. 2018, JGRA, 123, 1704
Cyr, O. C. S., & Webb, D. F. 1991, SoPh, 136, 379
Démoulin, P., & Aulanier, G. 2010, ApJ, 718, 1388
DeRosa, M. L., & Barnes, G. 2018, ApJ, 861, 131
DeRosa, M. L., Schrijver, C. J., Barnes, G., et al. 2009, ApJ, 696, 1780
Einaudi, G., & Hoven, G. V. 1983, SoPh, 88, 163
Falconer, D. A., Moore, R. L., & Gary, G. A. 2002, ApJ, 569, 1016
Fan, Y., & Gibson, S. E. 2007, ApJ, 668, 1232
Guo, Y., Ding, M. D., Schmieder, B., et al. 2010, ApJL, 725, L38
Hanssen, A. W., & Kuipers, W. J. A. 1965, MWRv, 81, 2
Harra, L. K., Schrijver, C. J., Janvier, M., et al. 2016, SoPh, 291, 1761
Harrison, R. 1995, A&A, 304, 585
Harrison, R. 2003, AdSpR, 32, 2425
Hills, M. 1966, Journal of the Royal Statistical Society: Series B (Methodological), 28, 1
Hood, A. W., & Priest, E. R. 1979, SoPh, 64, 303
Inoue, S., Hayashi, K., Magara, T., Choe, G. S., & Park, Y. D. 2014, ApJ, 788, 182
Inoue, S., Hayashi, K., Magara, T., Choe, G. S., & Park, Y. D. 2015, ApJ, 803, 73
Inoue, S., Hayashi, K., Shiota, D., Magara, T., & Choe, G. S. 2013, ApJ, 770, 79
Inoue, S., Kusano, K., Magara, T., Shiota, D., & Yamamoto, T. T. 2011, ApJ, 738, 161
Ishiguro, N., & Kusano, K. 2017, ApJ, 843, 101
Jing, J., Liu, C., Lee, J., et al. 2018, ApJ, 864, 138
Jing, J., Xu, Y., Lee, J., et al. 2015, RAA, 15, 1537
Kahler, S. W. 1992, ARA&A, 30, 113
Kahler, S. W., Sheeley, N. R., Jr., & Liggett, M. 1989, ApJ, 344, 1026
Kazachenko, M. D., Lynch, B. J., Welsch, B. T., & Sun, X. 2017, ApJ, 845, 49
Kliem, B., & Török, T. 2006, PhRvL, 96, 255002
Leka, K. D., & Barnes, G. 2003, ApJ, 595, 1296
Leka, K. D., & Barnes, G. 2007, ApJ, 656, 1173
Leka, K. D., Fan, Y., & Barnes, G. 2005, ApJ, 626, 1091
Lin, J., & Forbes, T. G. 2000, JGR, 105, 2375
Liu, Y. 2008, ApJL, 679, L151
Maričić, D., Vršnak, B., Stanger, A. L., et al. 2007, SoPh, 241, 99
Moore, R. L., Sterling, A. C., Hudson, H. S., & Lemen, J. R. 2001, ApJ, 552, 833
Möstl, C., Rollett, T., Frahm, R. A., et al. 2015, NatCo, 6, 7135
Muhamad, J., Kusano, K., Inoue, S., & Bamba, Y. 2018, ApJ, 863, 162
Nindos, A., Patsourakos, S., & Wiegelmann, T. 2012, ApJL, 748, L6
Priest, E., & Forbes, T. 2002, A&ARv, 10, 313
Qiu, J. 2009, ApJ, 692, 1110
Shiota, D., Kusano, K., Miyoshi, T., Nishikawa, N., & Shibata, K. 2008, JGRA, 113, A03S05
Sun, X., Bobra, M. G., Hoeksema, J. T., et al. 2015, ApJL, 804, L28
Temmer, M., Veronig, A. M., Vršnak, B., et al. 2008, ApJL, 673, L95
Thalmann, J. K., Su, Y., Temmer, M., & Veronig, A. M. 2015, ApJL, 801, L23
Toriumi, S., Schrijver, C. J., Harra, L. K., Hudson, H., & Nagashima, K. 2017, ApJ, 834, 56
Wang, D., Liu, R., Wang, Y., et al. 2017, ApJL, 843, L9
Wang, R., Liu, Y. D., Dai, X., et al. 2015, ApJ, 814, 80
Wang, Y., & Zhang, J. 2007, ApJ, 665, 1428
Wang, Y. M., Ye, P. Z., Wang, S., Zhou, G. P., & Wang, J. X. 2002, JGRA, 107, 1340
Yashiro, S., Gopalswamy, N., Akiyama, S., Michalek, G., & Howard, R. A. 2005, JGRA, 110, A12S05
Zhang, J., & Dere, K. 2006, ApJ, 649, 1100
Zhang, J., Dere, K. P., Howard, R. A., Kundu, M. R., & White, S. M. 2001, ApJ, 559, 452